



**HAL**  
open science

## **In vivo ultrasound modulated optical tomography with a persistent spectral hole burning filter**

Quang Minh Thai, Ghadir Kalot, Caroline Venet, Johanne Seguin, Maïmouna Bocoum, Nathalie Mignet, François Ramaz, Anne Louchet-Chauvet

### ► **To cite this version:**

Quang Minh Thai, Ghadir Kalot, Caroline Venet, Johanne Seguin, Maïmouna Bocoum, et al.. In vivo ultrasound modulated optical tomography with a persistent spectral hole burning filter. *Biomedical optics express*, 2022, 13, 10.1364/boe.475449 . hal-03903719

**HAL Id: hal-03903719**

**<https://hal.science/hal-03903719>**

Submitted on 16 Dec 2022

**HAL** is a multi-disciplinary open access archive for the deposit and dissemination of scientific research documents, whether they are published or not. The documents may come from teaching and research institutions in France or abroad, or from public or private research centers.

L'archive ouverte pluridisciplinaire **HAL**, est destinée au dépôt et à la diffusion de documents scientifiques de niveau recherche, publiés ou non, émanant des établissements d'enseignement et de recherche français ou étrangers, des laboratoires publics ou privés.



# *In vivo* ultrasound modulated optical tomography with a persistent spectral hole burning filter

QUANG MINH THAI,<sup>1</sup>  GHADIR KALOT,<sup>2</sup> CAROLINE VENET,<sup>1</sup>  
JOHANNE SEGUIN,<sup>2</sup>  MAÏMOUNA BOCOUM,<sup>1</sup>  NATHALIE MIGNET,<sup>2</sup>  
FRANÇOIS RAMAZ,<sup>1,\*</sup> AND ANNE LOUCHET-CHAUVET<sup>1,3</sup> 

<sup>1</sup>*Institut Langevin, ESPCI Paris, Université PSL, CNRS, 1 rue Jussieu, 75005 Paris, France*

<sup>2</sup>*Université de Paris Cité, INSERM, CNRS, UTCBS, Faculté de Pharmacie, 4 avenue de l'Observatoire, 75006 Paris, France*

<sup>3</sup>*anne.louchet-chauvet@espci.fr*

*\*Francois.Ramaz@espci.fr*

**Abstract:** We present *in vivo* ultrasound modulated optical tomography (UOT) results on mice, using the persistent spectral hole burning (PSHB) effect in a Tm<sup>3+</sup>:YAG crystal. Indocyanine green (ICG) solution was injected as an optical absorber and was clearly identified on the PSHB-UOT images, both in the muscle (following an intramuscular injection) and in the liver (following an intravenous injection). This demonstration also validates an experimental setup with an improved level of performance combined with an increased technological maturity compared to previous demonstrations.

© 2022 Optica Publishing Group under the terms of the [Optica Open Access Publishing Agreement](#) Optica Publishing Group

## 1. Introduction

Local optical properties of a biological tissue can provide useful information to improve medical diagnosis. Indeed, measuring the tissue's absorption coefficient, which is related to its vascular density or blood oxygenation level, has been identified as an efficient way to track tumor growth, brain activity or wound healing [1–3]. However, non-invasive optical imaging deep inside the tissue remains a challenge, because of strong light scattering, which results in low-resolution image at depths larger than a few mm. Coupling optical imaging to another imaging method capable of providing ballistic guidance, like ultrasound (US) imaging, was proposed as a solution to achieve high-resolution images of optical contrast deep inside the tissue. US modulated optical tomography (UOT) is an example of such a hybrid approach [4,5]: the acousto-optic effect between the US and the incident light generates modulated light (also known as “tagged light”), whose frequency is shifted by the US frequency. The tagged light is created within the insonified volume, and its intensity depends on the local absorption coefficient, which allows mapping of the optical contrast inside the tissue at the spatial resolution of the US – down to a hundred of micrometers at high US frequency. Furthermore, when using a linear US transducer similar to that used in standard ultrasound medical diagnosis, UOT can be included in a bimodal imaging solution, where both optical and mechanical contrast deep inside the tissue are accessible.

The challenge for UOT lies in the small ratio of tagged photons over incident photons: it is estimated between  $10^{-3}$  and  $10^{-4}$  [6], which leads to a low signal-to-noise ratio (SNR) of the image, since the unmodulated incident photons are merely a noise source in this case. To detect tagged photons, several approaches have been explored, namely laser speckle contrast [7,8], wavefront adaptive holography [9–11], US wavefront shaping [12–14], digital holography [14,15], spectral filtering approaches like Fabry-Perot interferometry [16,17] and spectral hole burning (SHB) narrowband filter [18–22]. Of all these methods, SHB filter provides both the

advantages of a high value of optical *etendue* and a deep, narrow spectral filter that is capable of significantly increasing the ratio of tagged light over background light, thus improving the SNR. Besides, as an incoherent filtering method, UOT is immune to the speckle decorrelation induced by the internal movement of scattering particles in the tissue, therefore more compatible with *in vivo* imaging.

Imaging tests on tissue-mimicking phantom and *ex vivo* animal tissue were reported in [18,19], using a  $\text{Tm}^{3+}$ :YAG crystal for SHB at 793 nm. Zhang *et al.*, Bengtsson *et al.* characterized and simulated the detection of acousto-optic signal on Intralipid phantom and animal tissue, using a  $\text{Pr}^{3+}$ : $\text{Y}_2\text{SiO}_5$  with SHB at 606 nm [20,21]. Venet *et al.* proposed to increase the depth and the lifetime of the  $\text{Tm}^{3+}$ :YAG transmission window with a magnetic field (also known as “persistent SHB” or PSHB), and demonstrated an improved imaging contrast compared to normal SHB filter, with experimental validation on Intralipid phantom with a low reduced scattering coefficient ( $\mu'_s = 1 \text{ cm}^{-1}$ ) [22]. However, the evaluation of these techniques for application in medical imaging is still missing, since to the best of our knowledge there is no complete *in vivo* UOT test to date: Lev *et al.* [23,24] performed a characterization of acousto-optic signal on *in vivo* samples (mice and human wrist/forearm), but it was limited to single-line signal acquisition, without a complete image and without any optical absorbers as imaging target. Therefore, it is necessary to establish a complete *in vivo* UOT test with SHB or PSHB filter, to evaluate its performance and identify elements to be optimized, opening the way towards the clinical implementation of UOT.

In this paper, we demonstrate *in vivo* PSHB-UOT in mice, using indocyanine green (ICG) solution - a medical dye with strong optical absorption at 793 nm (i.e. the wavelength of the laser used in the imaging setup) - as an optical absorber for imaging target, following both intramuscular and intravenous injections. The PSHB filter is created in a  $\text{Tm}^{3+}$ :YAG crystal under magnetic field. We also discuss, in parallel, some significant upgrades of the experimental setup which helped increasing the imaging quality of PSHB-UOT.

## 2. Experimental details

### 2.1. PSHB-UOT experimental setup

The experimental PSHB-UOT setup is depicted in Fig. 1. The output of a 793 nm laser diode (Toptica DL Pro) at frequency  $f_0$  is successively injected into an optical amplifier (Toptica BoosTA Pro) and to an acousto-optic deflector (AOD). The 1<sup>st</sup> order of diffraction of the AOD is sent to a cryogenically cooled  $\text{Tm}^{3+}$ :YAG crystal and burns a persistent spectral hole at the frequency of  $f_{p+} = f_0 + 80 \text{ MHz}$ . Unlike the pump cycle described in [21], with two spectral holes burned at  $f_{p-} = f_{probe} - f_{US}$  and  $f_{p+} = f_{probe} + f_{US}$ , here we generate only one spectral hole at the sideband frequency  $f_{p+}$  (Fig. 2(a)), for the same total pump duration. This is done to avoid the misalignment of the pump beam optical path, since the direction of the output diffracted beam from the AOD is highly sensitive to the modulated frequency. The crystal is a 2 mm thick,  $10 \times 10 \text{ mm}^2$  single YAG crystal doped with 2% at.  $\text{Tm}^{3+}$  ions (Scientific Materials Corp.), mounted inside a closed-cycle helium cryostat operating at 3.6 K (Cryostation – Montana Instruments). A permanent neodymium magnet is placed on top of the cryostat chamber to generate a 200 G vertical magnetic field, oriented along the [111] crystallographic axis of the  $\text{Tm}^{3+}$ :YAG crystal. The pump beam is vertically polarized, parallel to the magnetic field. The lifetime of spectral hole in  $\text{Tm}^{3+}$ :YAG in this configuration is estimated to be around 10 s at 3.6 K [25,26], making it necessary to refresh the spectral hole periodically.

The beam transmitted by the AOD (0<sup>th</sup> order) is coupled into an acousto-optic modulator (AOM) to generate the probe beam at frequency  $f_{probe} = f_0 + 75 \text{ MHz}$ , sent to the sample through a multimode optical fiber (200  $\mu\text{m}$  inner core diameter, NA = 0.39). We use a linear US transducer (Aixplorer Supersonic SL10-2), with 192 elements and 0.2 mm pitch, to generate focused US at 5 MHz, matching the frequency difference between the pump beam and probe beam. The lowest

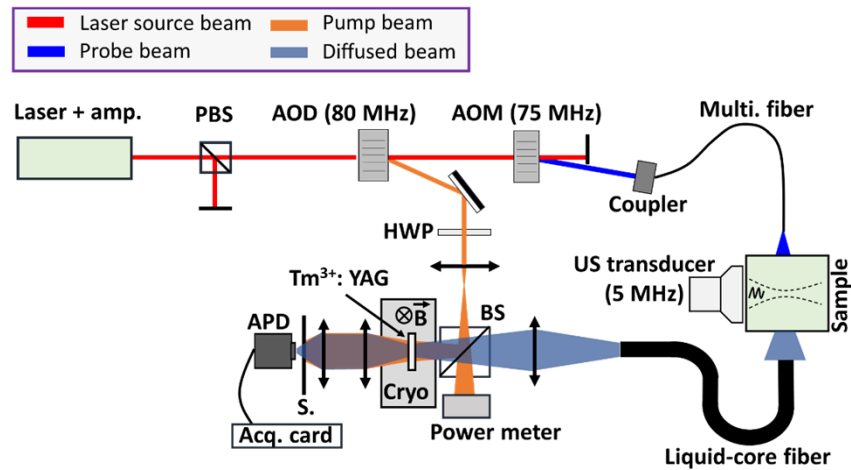


**Fig. 1.** Experimental setup for PSHB-UOT. Amp.: Optical amplifier. (P)BS: (Polarizing) beam splitter. AOD(M): Acousto-optic deflector (modulator). The use of a deflector allows for a large acousto-optic diffraction angle, which leads to an efficient isolation of the different orders of diffraction. Multi. Fiber: Multimode optical fiber. HWP: Half-wave plate. US transducer: Ultrasonic transducer. Cryo: Cryostat. S.: Shutter. APD: Avalanche photodiode. Acq. Card: Acquisition card.

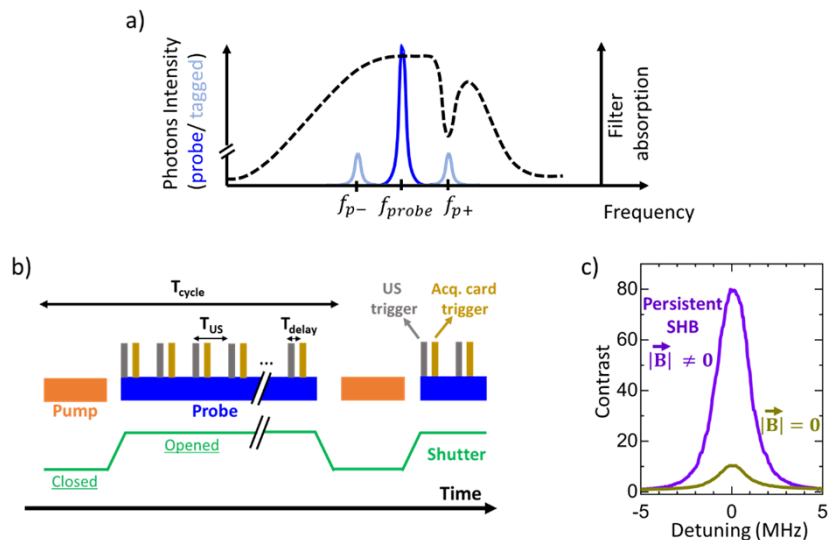


**Fig. 2.** a) SHB scheme using only one sideband of tagged photons. b) Experimental chronogram of pump-probe stage, along with the shutter status. Time scale is not respected. The cycle period  $T_{cycle}$  is 127 ms, and the delay  $T_{US}$  between two consecutive US pulses is 70  $\mu$ s. An additional delay  $T_{delay}$  of 8  $\mu$ s is added between each pair of US and acquisition card trigger, to match the beginning of each line acquisition with the start of US emission in the medium. c) The spectral hole contrast profile (see definition in text) measured with a chirped probe signal centered at the pump frequency, with and without magnetic field. The full width at half maximum (FWHM) is 2.1 MHz and 2.0 MHz., respectively.

possible lateral resolution of the US pulse is set by the pitch length, while the axial resolution depends on the number of US cycles in each pulse (here, at 5 MHz, the axial resolution is 0.31 mm per cycle, with the speed of sound taken as  $c = 1540$  m/s in water/Intralipid gel and in animal tissue). Light scattered from the sample (probe light and tagged light) is collected through a liquid-core fiber (8 mm inner core diameter, NA = 0.4) and combined with the pump beam to shine the  $\text{Tm}^{3+}$ :YAG crystal in a colinear configuration, thus ensuring maximal overlap between the two beams. A power meter is placed at the remaining port of the beam splitter (50:50 ratio) to measure the pump power illuminating the  $\text{Tm}^{3+}$ :YAG crystal. Light exiting the cryostat is then focused onto an avalanche photodiode (customized Hamamatsu C12703-01), connected to an acquisition card (Gage Digitizer CSE4344).

This colinear configuration requires to alternate between pumping stages, where the spectral hole is refreshed, and probing stages, where the UOT image is acquired. During the pumping stage, the APD must be protected from strong illumination (more than 100 mW transmitted through the cryostat) with a mechanical shutter (Uniblitz VS14). The chronogram of the experiment is shown in Fig. 2(b). The cycle period  $T_{\text{cycle}}$  is set to 127 ms, slightly longer than the minimum period allowed by the shutter controller (100 ms - Uniblitz VCM-D1). During the 10 ms-long pumping stage, the shutter is closed and the AOD is fed with a 80 MHz RF wave. The probing stage starts 3.2 ms after the end of the pumping stage, waiting for the shutter to be fully open. During the probing stage, the AOD is switched off, letting all the input optical power leak in the 0<sup>th</sup> order. The AOM is fed with a 75 MHz RF wave to generate a 9 ms-long probe pulse. 27 trigger signals are sent to the US transducer and the acquisition card, generating the US and starting the acquisition at each probing position. The delay  $T_{\text{US}}$  between each US trigger pulse is set to 70  $\mu\text{s}$ . The frequency shift and the duration of pump and probe stages are controlled through the waveforms sent into the AOD and AOM, using an arbitrary waveform generator (Tektronix AWG5004). Using a chirped signal centered at the pump frequency and swept on a 10 MHz range, we extracted the form of the spectral hole, with and without magnetic field (Fig. 2(c)): the presence of magnetic field generates indeed a spectral hole with a better contrast  $C = 80.0$ , compared to  $C = 10.4$  when the magnetic field is absent. Here, the contrast  $C(f)$  at a frequency  $f$  is defined as:  $C(f) = \frac{I(f) - I_{\text{bg}}}{I(f_{\text{probe}}) - I_{\text{bg}}}$ , with  $I(f)$ ,  $I(f_{\text{probe}})$ ,  $I_{\text{bg}}$  are respectively the optical signal at  $f$ ,  $f_{\text{probe}}$  and the background signal of the photodiode when no light arrives.

## 2.2. Sample preparation

We tested the PSHB-UOT technique first on a biological mimicking phantom, then on *ex vivo* and *in vivo* samples. The phantom was 24 mm thick made of Intralipid agar gel, with a reduced scattering coefficient  $\mu'_s = 10 \text{ cm}^{-1}$ , comparable to that of biological tissues. Two cylindrical optical absorbers made up of Intralipid mixed with black ink, of 1.4 mm diameter, separated by a 2 mm gap, were buried at the center of the phantom as imaging targets. The value of  $\mu'_s$  and the composition of the optical absorbers are similar to the one used in [22], with a comparable  $\text{Tm}^{3+}$ :YAG PSHB-UOT platform, allowing us to evaluate the performance of our current setup.

For PSHB-UOT test on animal tissues, we used bovine tissue for the *ex vivo* test, and six to eight weeks old living female BALB/cJrj mice (Janvier Labs, Le Genest Saint Isle, France) for *in vivo* tests. All the animal experiments were approved by the Animal Ethics Committee of the French Ministry (under the agreement number APAFIS 20344-2018080110035228) and were conducted according to European and national guidelines. The mice were anesthetized during the imaging session by intraperitoneal injection of Ketamine (100 mg/mL) and Xylazine (10 mg/mL) prior to the session. As an optical absorber for imaging target, we injected ICG at a concentration of 0.3 mg/mL. The absorption spectra of ICG are detailed in the Supplementary Information (Section S1 – Fig. S1).

Two types of *in vivo* imaging tests were conducted on mice: imaging of ICG after intramuscular injection into the thigh muscle (Fig. 3(a),(c)), and imaging of ICG accumulated in the liver

following intravenous injection, since ICG is cleared by the liver at a high rate after intravenous injection and it has been used to assess liver function in human [27] (Fig. 3(b),(d)). A catheter needle connected to a fixed Hamilton pump syringe (loaded with ICG) was used to perform the intramuscular injections into the thigh muscle. The injections (10-20  $\mu\text{L}$  of ICG at 0.3 mg/mL) were carried out by pushing the piston of the Hamilton syringe, guaranteeing the injection of a small amount of ICG without perturbing the position of the thigh muscle. The transmission configuration was used to image ICG in the thigh muscle. On the other hand, intravenous injection (200  $\mu\text{L}$  of ICG at 0.3 mg/mL) in the retro-orbital sinus was performed to image ICG accumulated in the liver. Imaging the liver in transmission configuration would have led to a very weak flux of scattered light due to the large abdominal volume of the mouse. To avoid this issue, we repositioned the incident multimode fiber and the collection liquid core fiber to collect light in a reflection configuration. In both imaging setups, the US transducer was adapted to work on small animals: we introduced a piece of agarose gel between the transducer surface and the tissue, so as to adjust the working distance to the optimal values of US transducer focal distance (from 20 mm onward) while maintaining mechanical contact. PSHB-UOT images were acquired before and after ICG injection to detect changes in the optical contrast. Intramuscular injection of ICG was also performed on a bovine tissue (10 mm thick), using the same imaging setup in transmission configuration, to compare with the *in vivo* results on mice. The mice thigh and belly were shaved for the intramuscular and intravenous injection tests, respectively, to ensure a good contact between the skin and the US transducer, with the aqua gel layer in between. The UOT images were collected up to 10 minutes after the intramuscular injection, and 45 minutes after the intravenous injection, with multiple repeated image acquisition to confirm the reproducibility of the results.

Given the fluorescence properties of ICG in the second near infrared (NIR-II) window (1000 nm -1700nm), whole body fluorescence imaging of the mice was conducted before and after ICG intramuscular/intravenous administration. It provided a further verification to the data obtained from PSHB-UOT. NIR-II fluorescence imaging of the mouse was performed using a Kaer Labs Imaging System, where a 808 nm laser excitation beam is focused on the mice, and the fluorescence emission is then detected using an InGaAs camera (NIRvana 640 ST, Teledyne Princeton Instruments). An adapted filter is used to block the laser light, letting only the fluorescence light captured by the camera. Bright field image of the mouse is acquired with an infrared LED as light source. Fluorescence imaging was performed after finishing the UOT imaging session (at least one hour after the intramuscular injection, or two hours after the intravenous injection of ICG).

Finally, we compare the levels of laser probe power arrived on the samples (Intralipid phantom and bovine/mice tissue) with the laser maximum permissible exposure (MPE) of the skin, according to the ANSI Z136.1 standard [28,29]:

$$MPE = 200 \times 10^{0.002(\lambda-700)} \text{ (mW.cm}^{-2}\text{)}$$

with  $\lambda$  the wavelength in nm. For  $\lambda = 793$  nm, it gives a MPE value of 307  $\text{mW.cm}^{-2}$ . For the test on Intralipid gel, on bovine tissue and on mouse thigh, we used laser probe power of 430 mW, 485 mW and 508 mW respectively, focused on a 1 cm-diameter spot on the sample, with a duty cycle  $D = 0.07$  ( $T_{\text{exposure}} = 9$  ms,  $T_{\text{cycle}} = 127$  ms). It corresponds to average powers of 38.8  $\text{mW.cm}^{-2}$ , 43.8  $\text{mW.cm}^{-2}$  and 45.8  $\text{mW.cm}^{-2}$ , well below the MPE threshold. For the UOT imaging on the liver, unfortunately we did not record the laser probe power during the test, but it is highly unlikely that it can surpass the MPE threshold, given the significant difference observed between the previous imaging test and the safety threshold.

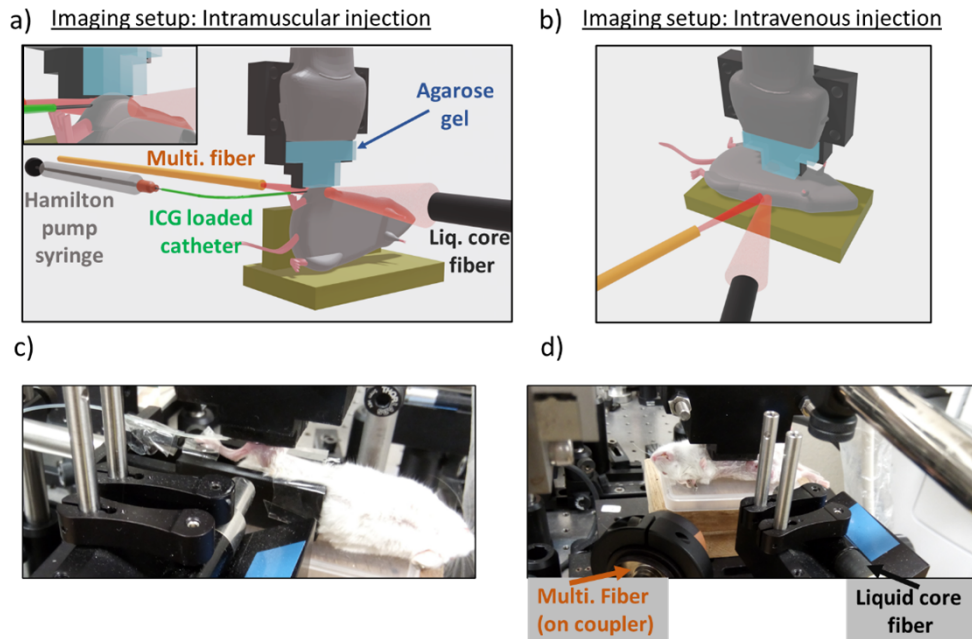


**Fig. 3.** Schematic presentation of PSHB-UOT setup for a) intramuscular injection of ICG in the thigh muscle (transmission configuration) and for b) intravenous injection of ICG to detect ICG accumulated in the liver (reflection configuration). A zoom on the contact between the agarose gel and the thigh muscle is shown in the inset of a). The front piece of the mechanical adapter (which hosts the US transducer and the agarose gel) and that of the mechanical support for the mouse body (in transmission configuration), along with the mechanical clamps for the multimode fiber, the liquid core fiber and the Hamilton pump syringe are not shown. The mouse body has a gray colour instead of white, for visualization purpose. c), d) Photos of the experimental setups for ICG c) intramuscular injection and d) intravenous injection PSHB-UOT tests, respectively. Only the coupler of the multimode fiber is shown, and the liquid core fiber is clamped on a mechanical holder (black piece with blue scotch glued upon on the image). The mouse is positioned on its side in the intramuscular injection test, and on its back in the intravenous test.

### 3. Results and discussions

#### 3.1. Calibration of PSHB-UOT performance on the intralipid phantom

We plot, in Fig. 4(a), the PSHB-UOT image of the Intralipid phantom (24 mm thick,  $\mu'_s = 10 \text{ cm}^{-1}$ ). The US pulse was set to 2 cycles, and 86 line-scans (0.2 mm step) were performed in the horizontal direction; each line was averaged 100 times, resulting in a total acquisition time  $T_{acq} = 40 \text{ s}$ . The vertical (Fig. 4(b)) and horizontal profiles (Fig. 4(c)) were extracted and fitted using gaussian functions (one for the envelope of diffused light and the others for optical absorbers). The FWHM values extracted from the vertical profile are 2.85 mm and 2.92 mm for the upper and lower absorber, respectively. The FWHM value for the lower absorber, extracted from the horizontal profile, is slightly higher (3.42 mm). Compared to the real diameter of the absorbers (1.4 mm - Fig. 4(d)), these values are significantly higher, similar to what was observed in [22].

In the following we compare the performance of the present experimental setup with that of the previous results reporting PSHB-UOT of Intralipid phantom (10 mm thick,  $\mu'_s = 10 \text{ cm}^{-1}$  [22]). Here, even with a much thicker sample, the maximum signal value increased significantly

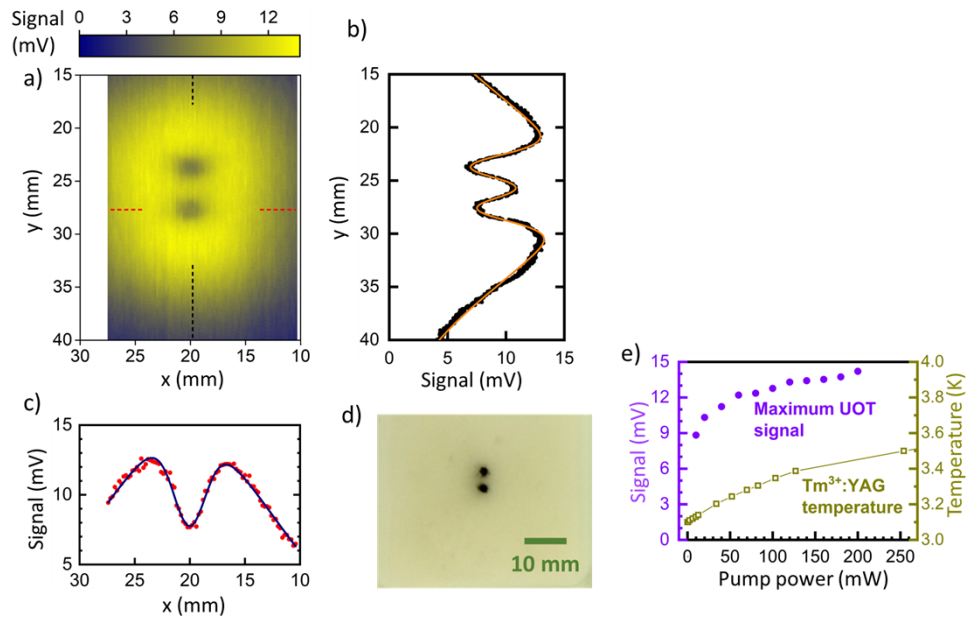


**Fig. 4.** a) PSHB-UOT image of the Intralipid phantom, with b) the vertical profile cut through both optical absorbers and c) the horizontal profile cut through the lower optical absorber. Raw data are shown in black and red dots, while gaussian fits are shown in orange and blue lines, respectively. d) Photo of the two absorbers in the Intralipid phantom. e) Maximum signal of PSHB-UOT images at different pump powers (magenta points), and the temperature of Tm<sup>3+</sup>:YAG crystal at different pump powers (dark yellow curve).

(13.7 mV compared to less than 5 mV in [22]), although both setups use a similar detector. Using the photosensitivity of the avalanche photodiode ( $1.5 \times 10^6$  V/W), these values correspond to 9.1 nW and 3.3 nW of tagged light optical power. Such an improvement was made possible by implementing several upgrades of the setup, that we describe in more detail. First, the *etendue* of the tagged light collection in the previous setup was estimated around 12 sr.mm<sup>2</sup>, and limited by the liquid helium cryostat windows [22]. In the present work, we use a closed-cycle cryostat that offers a wider optical access with an *etendue* of around 60 sr.mm<sup>2</sup>, such that the overall collection *etendue* is now limited by the liquid core fiber (8 mm inner diameter, acceptance angle of 31°, resulting in an optical *etendue* of 45 sr.mm<sup>2</sup>).

We then examine the effect of optical probe power on the sample, and the pump power on the Tm<sup>3+</sup>:YAG crystal. The probe power on the sample was estimated around 430 mW, i.e. more than twice that of the previous setup (200 mW). This leads to more tagged photons and thus increases the signal of the UOT image. We also measured the maximum signal of UOT image as a function of the pump power (Fig. 4(e)) and observed only a surprisingly slow increase in the tagged photons collection: an increase of the pump power from 60 to 200 mW leads to a 15% increase of the tagged signal. We attribute this observation to the competition between stronger light-matter interaction that should lead to a deeper spectral hole, and the laser-induced heating (see also in Fig. 4(e) for the plot of Tm<sup>3+</sup>:YAG crystal temperature as a function of pump power) that dramatically affects the spectral hole lifetime. This heating is typically expected in closed-cycle cryostats (see for example [30]), whose limited cooling power struggles to compensate for the fraction of the pumping power converted into heat in the Tm<sup>3+</sup>:YAG crystal. Accordingly, we set the peak pump power to 180 mW for imaging of the Intralipid phantom shown in Fig. 4(a), and for the in vivo imaging shown in the next section. Please note that the temperature values at

180 mW extracted from Fig. 4(e) (3.4 K) is slightly different than that during the UOT imaging sessions (3.6 K), which might be due to some small fluctuations of experimental condition between different tests, for example regarding how the pump beam is aligned on the  $\text{Tm}^{3+}$ :YAG crystal. The spectral hole lifetime is estimated around 10s at these temperatures.

It is also worth noting that the use of a different US transducer (linear transducer compared to single element transducer in [22]) might also influence the signal level of the PSHB-UOT image. However, we refrain from commenting further on the last remark, due to the lack of information regarding the values of acoustic pressure field used in the previous work.

### 3.2. *In vivo* PSHB-UOT

#### 3.2.1. Intramuscular injection of ICG in the mouse thigh

The results of *in vivo* PSHB-UOT of ICG intramuscular injection into the mouse thigh are shown in Fig. 5. By comparing the UOT images acquired before (Fig. 5(a) (i)) and after injection (Fig. 5(a) (ii)), we can identify the trace of injected ICG (20  $\mu\text{L}$ ), which is further illustrated by the cut section profile at  $x = 20$  mm (Fig. 5(b)), showing a local intensity drop due to the optical absorption of ICG. The stability of the mouse thigh position during the imaging session is verified by the similar form of the two UOT images, apart from the local intensity drop from ICG.

By projecting the PSHB-UOT image on the US image (Fig. 5(c) (ii)), one can observe a good overlap between the envelope of the UOT image (Fig. 5(a) (ii)) and the US image (Fig. 5(c) (i)) of the thigh muscle. The part of the muscle between  $x = 10$  mm and  $x = 15$  mm is not displayed on the UOT images since it was not covered by the incident laser beam (approximately 10 mm in diameter). It is worth noting that it is difficult to identify with high fidelity the trace of the catheter needle on the UOT images (Fig. 5(a)). This might be due to a tilted orientation of the needle compared to the vertical plan, where the propagation of US takes place: as seen in the US image (Fig. 5(c) (i)) we can only identify the tip of the needle inserted in the muscle. Nevertheless, the position of the ICG trace still shows a good overlap with the apex of the needle (Fig. 5(c) (ii)); the presence of ICG is further verified by the fluorescence image acquired after injection, with clear fluorescence signal observed at the thigh muscle (Fig. 5(d) (iii)). A second test for intramuscular injection of ICG in the thigh of a different mouse (see Fig. S2 in Supplementary Information) was performed, showing similar results (ICG trace is detected, but once again the needle could not be clearly identified) and illustrating the technical difficulties for UOT imaging on small *in vivo* samples. Given a bigger, more uniform animal tissue sample, it would be easier to achieve a good orientation of the needle and identify it on the UOT image. We show an example of such case in Fig. 6, with PSHB-UOT images for ICG injection into an *ex vivo* bovine tissue: one can easily identify the needle before the injection on the UOT images, and the needle with ICG trace on its apex after the injection.

#### 3.2.2. Imaging of ICG accumulating in the liver after an intravenous injection

The results of PSHB-UOT on the mouse liver following an intravenous injection of ICG are shown in Fig. 7: UOT images acquired before (Fig. 7(a) (i)) and after the injection (Fig. 7(a) (ii)) show a clear difference, with an intensity drop detected over a large area, suggesting indeed the presence of ICG in the liver. This is further confirmed by looking at the signals along the vertical profile at  $x = 19$  mm (Fig. 7(b)). The upper part in the UOT images (around  $y = 27$  mm) does not show a significant change, since it corresponds to the belly skin covering the abdominal region. It is interesting to note that there is also another region of the image (long line, near  $x = 15$  mm, between  $y = 35$  mm and  $y = 40$  mm) with a strong signal that was not affected by the ICG injection. It might be due to an artefact during the acquisition of UOT images, but we do not have yet a certain explanation for this phenomenon. We project the UOT image acquired after injection on the US image, and observe that the region of intensity drop matches the position of the liver (Fig. 7(c) (ii)). Fluorescence images acquired before and after ICG injection (Fig. 7(d) (ii), (iii))

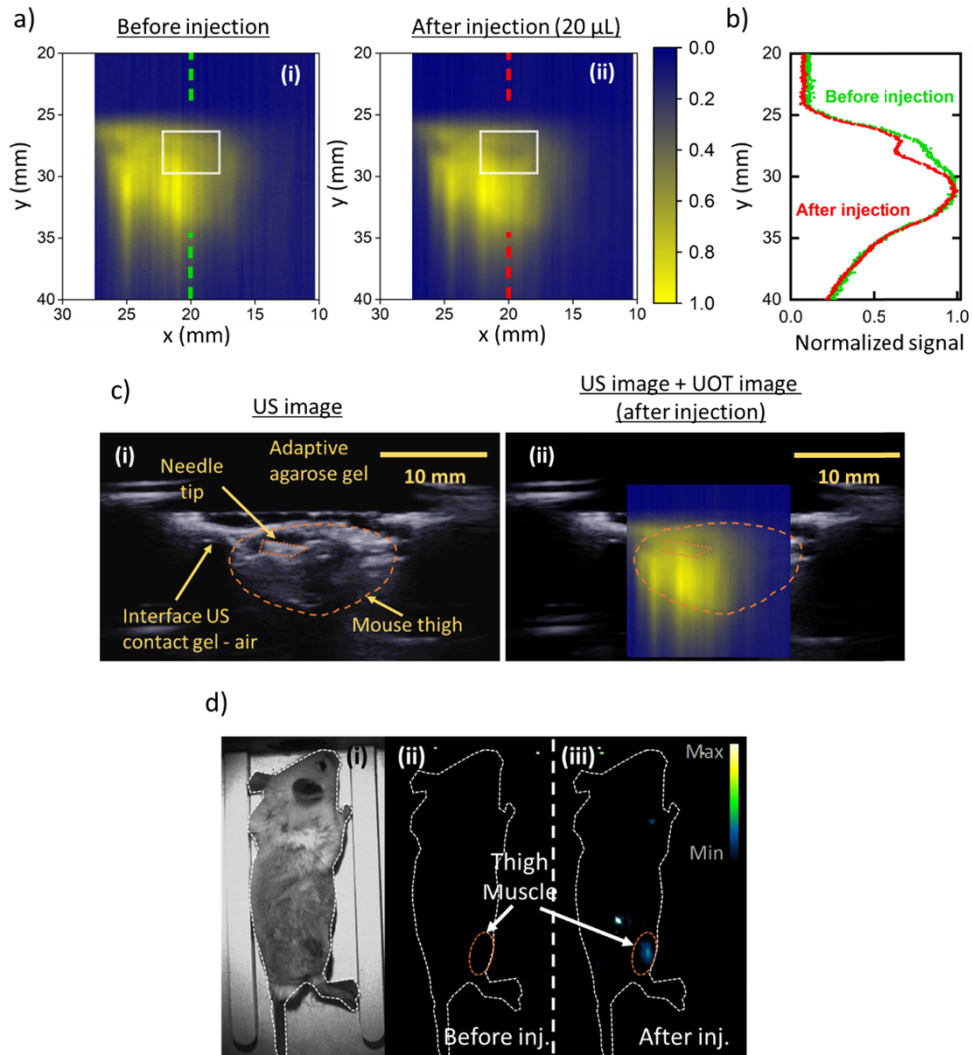


**Fig. 5.** a) PSHB-UOT images before (i) and after (ii) ICG injection (20  $\mu\text{L}$ ) into the mouse thigh muscle. The signal of each image is normalized. The white boxes help locating the intensity drop due to the optical absorption of ICG b) Vertical profiles at  $x = 20$  mm before and after ICG injection, showing a clear intensity drop at  $y = 28$  mm. c) US image alone (i), and US image with UOT image (ii) (after ICG injection) projected on it. The needle tip and the mouse thigh are marked in orange contours. In the US image, the diameter of the needle appears larger than its real diameter ( $\sim 1$  mm compared to 0.4 mm). d) Bright field image (i) and whole body NIR-II fluorescence images of mouse (side position) acquired before (ii) and after ICG injection (iii), with the latter showing a clear fluorescence signal of ICG trace in the thigh muscle

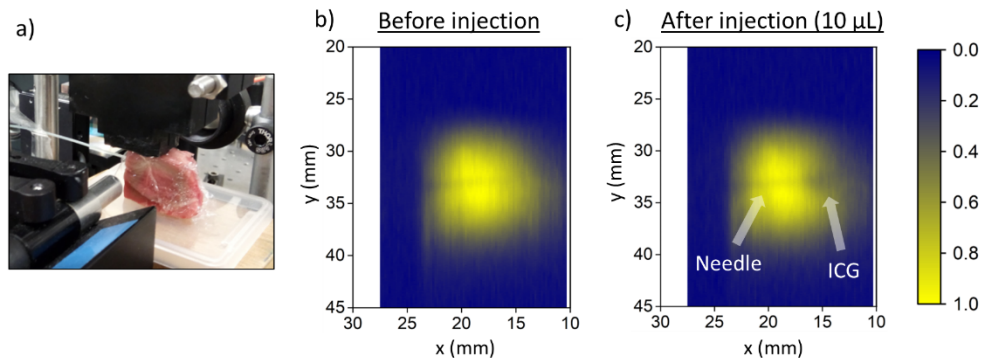


**Fig. 6.** a) Photo of PSHB-UOT imaging setup for ICG injection into bovine tissue (10 mm thick). b) PSHB-UOT image taken before ICG injection, showing the presence of the needle (faint blue line) inside the tissue c) PSHB-UOT image taken after the injection of ICG (10 μL), showing the presence of the needle and the ICG trace held on its apex. The signal of each UOT image is normalized.

also show a clear contrast, with a strong fluorescence signal observed in the mouse abdominal region after injection, originating from the accumulation of ICG in the liver. Additional imaging tests on two liver sections sampled from a different sacrificed mouse, with and without ICG injection also show a clear difference in contrast (see Fig. S3 in Supplementary Information) and validate further the results from *in vivo* PSHB-UOT tests. It is worth noting that in both *in vivo* imaging experiments (on mouse thigh and liver) shown in this work, the small size of the mouse thigh and the close distance between the liver and the belly skin layer make fluorescence imaging an excellent tool to verify results from UOT imaging, retaining a good resolution. In a much thicker sample (see Fig. S3c in Supplementary Information), scattering effect will become more important and will degrade the resolution of the fluorescence image, compared to the UOT image.

These results demonstrated the potential of PSHB-UOT for *in vivo* imaging and tracking of metabolic processes deep inside the tissue. Regarding future work in this topic, one might follow a similar research direction as the one intensively explored in photoacoustic imaging [31,32], which focuses on using optical absorptive contrast agents specifically designed to target abnormal or mutated cell. For example, by injecting a tumor-targeted marker with strong optical absorption in the NIR wavelength into tumor-bearing mice [33], the PSHB-UOT shown in this work can be used to track the tumors growth. Finally, it should be noted that many aspects of the current PSHB-UOT setup are subject to further optimization, aiming for images of higher quality: for example, the tagged light intensity could be increased by using a higher intensity probe beam while still complying with safety regulations, or with the use of structured US waves [12,13]. An important development towards practical PSHB-UOT imaging for long-term future clinical test on humans will be to build appropriate mechanical holders combining illumination and collection fibers together with the US probe; designs for these holders can be inspired by systems that have been developed in the field of photoacoustic imaging [34,35]. Such holders would also need to be specific for tests on different human body parts (tracking of breast and liver tumor, for example).

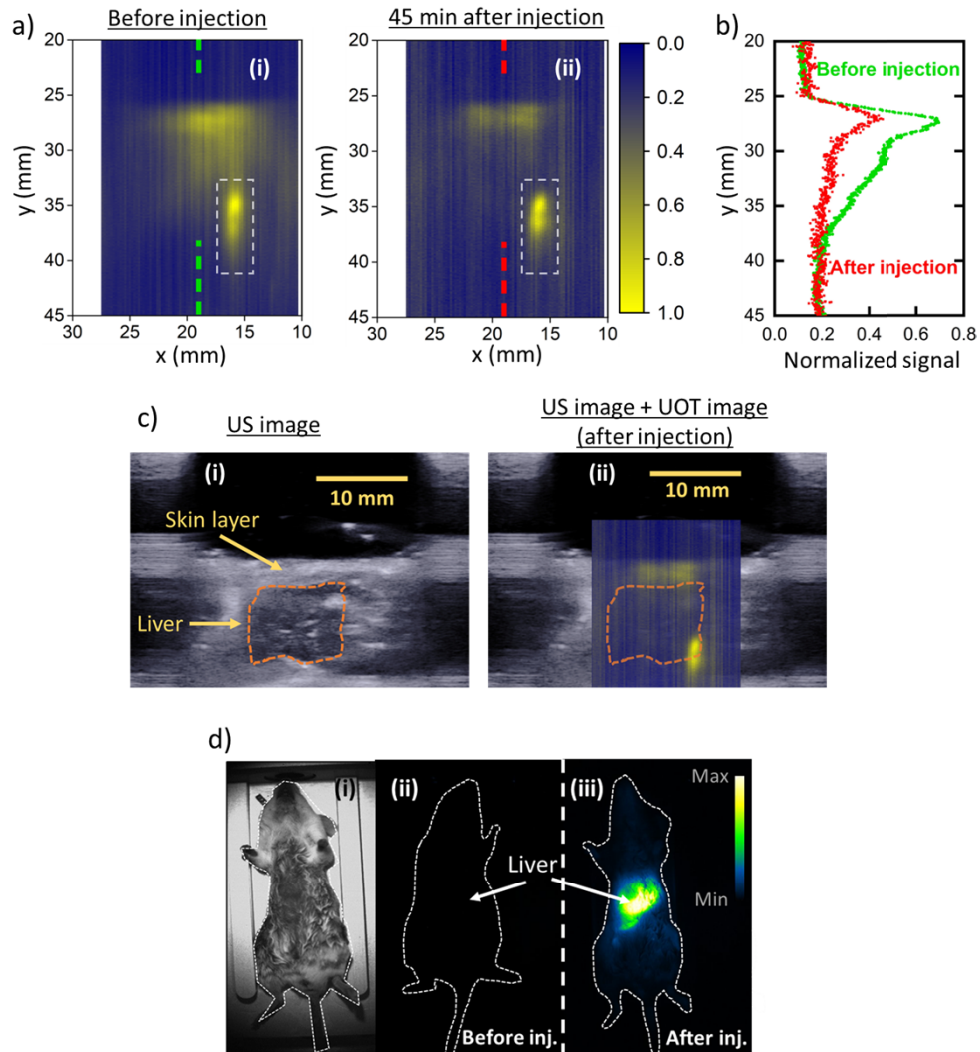


**Fig. 7.** a) PSHB-UOT images taken for a vertical section of the mouse liver before (i) and 45 min after (ii) the intravenous injection of ICG. The area of strong artefact signal is marked with dashed white boxes in both UOT images. b) Vertical profiles at  $x = 19$  mm before and 45 min after intravenous ICG injection, showing a strong intensity drop from  $y = 27$  mm onwards. c) US image alone (i), and US image with the projected UOT image (45 min after ICG injection) (ii). The mouse liver is marked in orange contour. The liver is present between the lung (left side of the image) and the intestinal tract (right side of the image) d) Bright field image (i) and whole body NIR-II fluorescence images of mouse (ventral position) acquired before (ii) and after the injection (iii), showing a clear accumulation of ICG in the liver. Note that these fluorescence images show the entire liver of the mouse, whereas the UOT images show only a cut section of the liver.

#### 4. Conclusion

In this work we demonstrated the first *in vivo* PSHB-UOT images on mice, with ICG injected as an optical absorber for imaging target. The traces of ICG in the thigh muscle (following an intramuscular injection) and ICG accumulating in the liver (following an intravenous injection) were clearly observed on the UOT images. These experiments validate the increased technologic maturity of our experimental setup that uses a standard closed-cycle cryostat and a commercial, free running semiconductor laser. It also provides a framework for future *in vivo* UOT tests, among which tracking tumor growth using tumor-targeted contrast agents will be a prioritized direction.

**Funding.** Agence Nationale de la Recherche (France Life Imaging ANR-11-INBS-0006); Fondation ARC pour la Recherche sur le Cancer (ARCPST-DOC2021080004118).

**Acknowledgements.** The authors acknowledge the support from the “Investissements d’Avenir” program, from a France Life Imaging grant (ANR-11-INBS-0006), and finally the “Fondation ARC pour la recherche sur le cancer (Fondation ARC)” for its specific support for G.K. (ARCPST-DOC2021080004118). We also acknowledge Louis Dutheil from Institut Langevin for his help in preparing the Intralipid tissue-mimicking phantom, and Cyrille Richard from UTCBS laboratory for his help in preparing the ICG solution. We also thank the imaging facility LIOPA - Plateformes d’Imageries du Vivant PIV, Université de Paris Cité, CNRS UMS3612 Inserm US25 for allowing the use of their fluorescence imaging setup for this work.

**Disclosures.** The authors declare no conflicts of interest.

**Data availability.** Data underlying the results presented in this paper are not publicly available at this time but may be obtained from the authors upon reasonable request.

**Supplemental document.** See [Supplement 1](#) for supporting content.

#### References

1. D. Grosenick, H. Wabnitz, K. T. Moesta, J. Mucke, P. M. Schlag, and H. Rinneberg, “Time-domain scanning optical mammography: II. Optical properties and tissue parameters of 87 carcinomas,” *Phys. Med. Biol.* **50**(11), 2451–2468 (2005).
2. H. F. Zhang, K. Maslov, G. Stoica, and L. V. Wang, “Functional photoacoustic microscopy for high-resolution and non invasive *in vivo* imaging,” *Nat. Biotechnol.* **24**(7), 848–851 (2006).
3. J. Yao, K. Maslov, Y. Zhang, Y. Xia, and L. V. Wang, “Label-free oxygen-metabolic photoacoustic microscopy *in vivo*,” *J. Biomed. Opt.* **16**(7), 076003 (2011).
4. L. V. Wang, “Mechanisms of ultrasonic modulation of multiply scattered coherent light: an analytic model,” *Phys. Rev. Lett.* **87**(4), 043903 (2001).
5. S. G. Resink, A. C. Boccara, and W. Steenbergen, “State-of-the art of acousto-optic sensing and imaging of turbid media,” *J. Biomed. Opt.* **17**(4), 040901 (2012).
6. G. D. Mahan, W. E. Engler, J. J. Tiemann, and E. Uzgiris, “Ultrasonic tagging of light: theory,” *Proc. Natl. Acad. Sci. U. S. A.* **95**(24), 14015–14019 (1998).
7. S. Leveque, A. C. Boccara, M. Lebec, and H. Saint-Jalmes, “Ultrasonic tagging of photon paths in scattering media: parallel speckle modulation processing,” *Opt. Lett.* **24**(3), 181–183 (1999).
8. J. Li, G. Ku, and L. V. Wang, “Ultrasound-modulated optical tomography of biological tissue by use of contrast of laser speckles,” *Appl. Opt.* **41**(28), 6030–6035 (2002).
9. F. Ramaz, B. C. Forget, M. Atlan, A. C. Boccara, M. Gross, P. Delaye, and G. Roosen, “Photorefractive detection of tagged photons in ultrasound modulated optical tomography of thick biological tissues,” *Opt. Express* **12**(22), 5469–5474 (2004).
10. S. Farahi, E. Benoit la Guillaume, A. A. Grabar, J.-P. Huignard, and F. Ramaz, “Time resolved three-dimensional acousto-optic imaging of thick scattering media,” *Opt. Lett.* **37**(13), 2754–2756 (2012).
11. J.-B. Laudereau, E. Benoit la Guillaume, V. Servois, P. Mariani, A. A. Grabar, M. Tanter, J.-L. Gennisson, and F. Ramaz, “Multi-modal acousto-optic/ultrasound imaging of *ex vivo* liver tumors at 790 nm using a Sn2P2S6 wavefront adaptive holographic setup,” *J. Biophotonics* **8**(5), 429–436 (2015).
12. M. Bocoum, J.-L. Gennisson, J.-B. Laudereau, A. Louchet-Chauvet, J.-M. Tualle, and F. Ramaz, “Structured ultrasound-modulated optical tomography,” *Appl. Opt.* **58**(8), 1933–1940 (2019).
13. M. Bocoum, J.-L. Gennisson, A. A. Grabar, F. Ramaz, and J.-M. Tualle, “Reconstruction of bi-dimensional images in Fourier-transform acousto-optic imaging,” *Opt. Lett.* **45**(17), 4855–4858 (2020).
14. L. Dutheil, M. Bocoum, M. Fink, S. M. Popoff, F. Ramaz, and J.-M. Tualle, “Fourier transform acousto-optic imaging with off-axis holographic detection,” *Appl. Opt.* **60**(24), 7107–7112 (2021).
15. M. Gross, P. Goy, and M. Al-Koussa, “Shot-noise detection of ultrasound-tagged photons in ultrasound-modulated optical imaging,” *Opt. Lett.* **28**(24), 2482–2484 (2003).

16. S. Sakadzic and L. V. Wang, "High-resolution ultrasound-modulated optical tomography in biological tissues," *Opt. Lett.* **29**(23), 2770 (2004).
17. G. Rousseau, A. Blouin, and J.-P. Monchalain, "Ultrasound-modulated optical imaging using a high-power pulsed laser and a double-pass confocal Fabry–Perot interferometer," *Opt. Lett.* **34**(21), 3445 (2009).
18. Y. Li, H. Zhang, C. Kim, K. H. Wagner, P. Hemmer, and L. V. Wang, "Pulsed ultrasound-modulated optical tomography using spectral-hole burning as a narrowband spectral filter," *Appl. Phys. Lett.* **93**(1), 011111 (2008).
19. X. Xu, S.-R. Kothapalli, H. Liu, and L. V. Wang, "Spectral hole burning for ultrasound-modulated optical tomography of thick tissue," *J. Biomed. Opt.* **15**(6), 066018 (2010).
20. H. Zhang, M. Sabooni, L. Rippe, C. Kim, S. Kroll, L. V. Wang, and P. Hemmer, "Slow light for deep tissue imaging with ultrasound modulation," *Appl. Phys. Lett.* **100**(13), 131102–1 (2012).
21. A. Bengtsson, D. Hill, M. Li, M. Di, M. Cinthio, T. Erlov, S. Andresson-Engels, N. Reistad, A. Walther, L. Rippe, and S. Kroll, "Characterization and modeling of acousto-optic signal strengths in highly scattering media," *Biomed. Opt. Express* **10**(11), 5565 (2019).
22. C. Venet, M. Bocoum, J.-B. Laudereau, T. Chaneliere, F. Ramaz, and A. Louchet-Chauvet, "Ultrasound-modulated optical tomography in scattering media : flux filtering based on persistent spectral hole burning in the optical diagnosis window," *Opt. Lett.* **43**(16), 3993–3996 (2018).
23. A. Lev and B. Sfez, "In vivo demonstration of the ultrasound modulated light technique," *J. Opt. Soc. Am. A* **20**(12), 2347 (2003).
24. A. Lev, E. Rubanov, B. Sfez, S. Shany, and A. J. Foldes, "Ultrasound-modulated light tomography assessment of osteoporosis," *Opt. Lett.* **30**(13), 1692–1694 (2005).
25. L. Veissier, C. W. Thiel, T. Lutz, P. E. Barclay, W. Tittel, and R. L. Cone, "Quadratic Zeeman effect and spin-lattice relaxation of  $Tm^{3+}$ :YAG at high magnetic fields," *Phys. Rev. B* **94**(20), 205133 (2016).
26. A. Louchet-Chauvet, "*Processeurs atomiques pour le traitement de signaux optiques et radio-fréquence*," Université Paris-Sud (2019).
27. A. De Gasperi, E. Mazza, and M. Prosperi, "Indocyanine green kinetics to assess liver function: Ready for a clinical dynamic assessment in major liver surgery?" *WJH* **8**(7), 355–367 (2016).
28. ANSI Z136.1 - Safe Use of Lasers (American National Standard, 2014).
29. A. K. Maini, "Appendix A: Laser Safety," in *Lasers and Optoelectronics: Fundamentals, Devices and Applications* (Wiley, 2013).
30. T. Hasebe, S. Okada, M. Ishizuka, T. Tsurudome, T. Ito, H. Ookubo, J. Sakuraba, K. Watanabe, S. Awaji, K. Koyama, G. Nishijima, and K. Takahashi, "Design of a cryocooler-cooled large bore superconducting magnet for a 30 T hybrid magnet," *IEEE Trans. Appl. Supercond.* **14**(2), 368–371 (2004).
31. J. Xia, J. Yao, and L. V. Wang, "Photoacoustic tomography: principles and advances," *Prog. Electromagn. Res.* **147**, 1–22 (2014).
32. J. Yao and L. V. Wang, "Sensitivity of photoacoustic microscopy," *Photoacoustics* **2**(2), 87–101 (2014).
33. A. Godard, G. Kalot, J. Pliquett, B. Busser, X. Le Guével, K. D. Wegner, U. Resch-Genger, Y. Rousselin, J.-L. Coll, F. Denat, E. Bodio, C. Goze, and L. Sancey, "Water-soluble Aza-BODIPYs: biocompatible organic dyes for high contrast in vivo NIR-II imaging," *Bioconjugate Chem.* **31**(4), 1088–1092 (2020).
34. L. V. Wang and J. Yao, "A practical guide to photoacoustic tomography in the life sciences," *Nat. Methods* **13**(8), 627–638 (2016).
35. L. Lin, X. Tong, P. Hu, M. Invernizzi, L. Lai, and L. V. Wang, "Photoacoustic computed tomography of breast cancer in response to neoadjuvant chemotherapy," *Adv. Sci.* **8**(7), 2003396 (2021).